UNIVERSITY OF
BATH

University of Bath

Alternative formats
If you require this document in an alternative format, please contact:
openaccess@bath.ac.uk
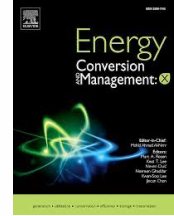
Full Length Article

Design, simulation, and validation of additively manufactured high-temperature combustion chambers for micro gas turbines

Adamos Adamou[a]*, James Turner[a], Aaron Costall[a], Andy Jones[b], Colin Copeland[c]

[a] *Institute for Advanced Automotive Propulsion Systems (IAAPS), University of Bath, Claverton Down, Bath, BA2 7AY, United Kingdom*
[b]*HiETA Technologies Ltd., Bristol & Bath Science Park, Dirac Crescent, Emersons Green, Bristol, BS16 7FR*
[c]*School of Sustainable Energy Engineering, Simon Fraser University, 10285 University Dr, Surrey, BC V3T 4B7, Canada*

ARTICLE INFO

ABSTRACT

The demand for cleaner, more efficient, and durable sources of electricity is driving research into small-scale power generation. Micro gas turbines are especially suitable by virtue of their high power density and reliability, but a major drawback is their poor overall efficiency due to increasing parasitic energy losses relative to net power output as size decreases. Additive manufacturing offers design freedoms that could enable higher efficiency and lower emission combustors for micro gas turbine applications. A novel conical radial swirl-stabilized tubular combustor with internal vane fuel injection is designed and tested, and a validated reacting computational fluid dynamics model is used to design novel combustor features that can only be additively manufactured. Of the five different concepts tested, those benefitting from additively manufactured features outperform the traditional design in terms of peak temperature control and fuel-air mixing, translating to striking reductions in pollutant emissions, with up to 75% and 40% reductions in nitrogen oxides and carbon monoxides, respectively, while concepts incorporating upstream fuelling and a three-row lattice show a near 20% increase in mixture quality. As well as evaluating a number of novel and very promising additively manufactured combustor design features, this work provides guidance on the incorporation of additively manufactured features in combustors for any gas turbine application and demonstrates the clear benefits of additive manufacturing for low-emission combustor design.

1. Introduction

Despite increasing development of renewable energy sources for electricity generation, the conventional internal combustion engine remains the only realistic choice in many applications. Such applications include remote power for telecommunication equipment in regions where renewables are not yet viable, and small combined heat and power (CHP) systems for commercial and residential buildings. Internal combustion engines are also commonly found in the unmanned aerial vehicle (UAV) industry, and they remain the predominant prime mover in ground transport

applications. Such prevalence is due to low upfront and fuel costs combined with acceptable efficiency, although maintenance requirements can contribute to higher total owning and operating costs in comparison to alternatives. One such alternative is the micro gas turbine (MGT), which offers many benefits: flexible multi-fuel (both gaseous and liquid) operation, fewer moving parts and hence lower maintenance requirements, lower noise, and, if designed correctly, significantly reduced emissions.

1.1. Micro gas turbine applications

Currently, many ongoing projects are developing micro gas turbines for small-scale power generating units in the 100 kWe range and below, for

various applications in different markets. Examples of these projects include the conversion of an MTT EnerTwin for residential use by adapting it to operate on an inverted Brayton cycle, by doing so eliminating the need to pressurize the existing residential natural gas feed [1]. The ARPA-E GENSETS program, which is aiming to develop small natural gas-fuelled combined heat and power units for residential use, has several projects developing MGT systems [2]. MGTs running on biofuels are also gaining popularity due to the desire to use alternative fuels that enable lower lifecycle carbon dioxide (CO_2) emissions [3]. Interesting research is also being conducted on micro gas turbines for micro electro mechanical systems in the 10-50 W range [4].

The drone market has also seen several MGT units in development. This is due to the demand for quieter, lighter, and more efficient engines to replace the commonly used piston engine. Examples of such projects include the US Navy Black Ghost, a sub-20 kW engine for small drones that incorporates a ceramic recuperated combustion chamber [5], and the Monarch 5, which has been developed by UAV Turbines for powering a turboprop system or working as a range extender for small electrical hybrid aerial vehicles [6]. The automotive and heavy vehicle industry is also developing MGTs for use as range extenders in various types of hybrid electric vehicles such as waste disposal trucks, buses, and delivery vans; in this area, Wrightspeed has been developing powertrains for some years now [7]. On the smaller side, the Ariel Motor Company is developing the P40, an electric and micro gas turbine hybrid HIPERCAR, using a gas turbine being developed by Delta Motorsports. The initial research for its combustion chamber was conducted in the University of Bath's Institute of Advanced Automotive Propulsion Systems (IAAPS) [8].

The proliferation of such projects is due to MGT attributes that are attractive in many applications, which include reduced service requirements (from fewer moving parts), minimal lubrication requirements, and their ability to achieve significantly lower emissions than an equivalent reciprocating combustion engine. Additionally, concerning the challenges of future transportation, the ability of the gas turbine to operate on a wide range of fuels could be very important. Specifically, hydrogen can easily be burnt in a gas turbine, which eliminates exhaust CO_2 emissions during normal operation as well as the hydrocarbon and carbon monoxide emissions at start-up. Since the latter two are especially challenging this could be a major advantage as air quality requirements tighten.

Due to their relatively low overall energy conversion efficiency though, there has been a hesitation to adopt MGT technology over conventional reciprocating engines. However, a few examples do exist. These include the MTT EnerTwin unit, which has a 16% electrical efficiency at 3.2 kWe [9], the Bladon Jets 12 kWe turbine with an efficiency of 25% [10], and the Capstone C65 with 29% electrical efficiency [11]. These low efficiencies are mainly due to commonly occurring losses, such as friction, heat dissipation, and leakage, but which take on greater importance in MGTs since the proportion of the total power they account for is inversely proportional to turbine size, becoming quite substantial at power ranges below 100 kWe. In the case of leakage, for example, this is because the relevant design parameters, viz. clearances and manufacturing tolerances, do not scale with overall size but rather are fixed absolute values.

1.2. Additively manufactured combustion chambers

Additive manufacturing (AM) has become very useful for MGTs since small-scale intricate features and designs can now be used to reduce some of the common sources of energy loss. Although the use of AM in MGT combustion chambers is relatively new, there are a number of completed and in-flight projects in the industrial and aerospace gas turbine sector. Notable examples include General Electric's LEAP fuel injector [12], the EOS Euro-K multi-fuel micro burner [13], and the Siemens pre-mixer for the SGT-A05 [14]. Additionally, Siemens developed a method of using AM technology to repair their DLE (dry low emission) burners for the SGT-700 and SGT-800 engines, involving removal of the damaged injector tip and inserting it into a printer to create the new tip [15]. Research conducted at lower levels of technology readiness investigated additively manufactured porous structures for cooling [16] and flame stabilization [17].

The use of AM for combustion chambers is not limited to the gas turbine industry. Research is being conducted for its use in rocket engines, for example NASA's AM copper alloy combustion chamber [18], and in combination with artificial intelligence to create combustion chamber designs that were previously unimaginable, such as the cooled rocket engine combustor by Hyperganic [19].

1.3. Research gap, hypothesis, and objectives

Due to the small size of MGT combustion chambers, it is very difficult to realize significant improvements based on traditional manufacturing techniques. Additive manufacturing can bypass such manufacturing limitations to provide the accuracy and flexibility required. And while various low emissions combustion technologies exist, even for micro gas turbines, there is a clear lack of research investigating the potential of additive manufacturing to further improve these technologies. The publications that are available on the aforementioned projects involving additively manufactured combustor components, such as General Electric's LEAP fuel injector [12], the EOS Euro-K multi-fuel micro burner [13], and the Siemens pre-mixer for the SGT-A05 [14], are rather superficial and do not convey sufficient detail to be useful to the wider research and development of combustors for MGTs. On the other hand, the research that is transparent enough, such as the work by Fantozzi et al. [16] and Samoilenko et al. [17], generally lies at very low technology readiness levels, is yet to be tested in full-scale systems, and so would require substantial further research to be applicable to current MGT demands.

Thus, there exists a research gap in terms of high technology readiness level applications of AM in combustion chambers. For example, this could include exploiting the design freedoms available through AM to develop novel cooling schemes that permit operation at higher gas temperatures, thereby enabling greater thermal efficiency. Concurrently, the minimization of pollutant emissions could benefit from low pressure loss fuel-air mixing devices that exploit additively manufactured designs.

So, the research hypothesis is that additive manufacturing offers design freedoms that could enable higher efficiency and lower emission combustors for micro gas turbine applications. Hence this research program aimed to develop a combustion chamber that takes advantage of such design freedoms to meet a set of specifications for a MGT having an overall 40% electrical efficiency. Although the combustion chamber is not the only

part required to achieve such high efficiency, all the major design parameters for the system can be deduced from combustion targets. At the outset of the research project, a set of specifications was developed to help guide the work and set the metrics for success; these are shown in Table 1.

Table 1 – Target Specification

Specifications	Values	Units
Power capacity	10	kW
Electrical efficiency	40	%
Air mass flow rate	70	g/s
Inlet temperature	820	ºC
Outlet temperature	1250	ºC
Inlet air pressure	400	kPa
Pressure drop	<3	% of inlet
Nitrous oxides (NOx)	<10	ppm
Carbon monoxides (CO)	<20	ppm
Service life	40000	Hours
Fuel	Natural Gas	

1.4. Layout of this article

Having introduced the work, the subsequent sections are as follows:

- Sec. 2: *Design and analysis of baseline combustion chamber*, justifies the initial design decisions for the type of combustion chamber, fuel injection, and flame stabilization, and describes potential issues that may require AM solutions to meet the required combustor performance specifications.
- Sec. 3: *Additively manufactured features*, describes the analytical design process, illustrating how the initial concept was created using empirical calculations. A short discussion on design guidelines for AM is presented, followed by a description of the various features implemented in the baseline design, what each of the features achieves, and how to build them in AM.
- In Sec. 4: *Baseline reacting CFD, manufacturing and validation,* a reacting CFD model is validated against test results for the baseline design and is used to assess the effects of its AM-enabled design adaptations. It also discusses the equipment, materials, and process parameters used to create the baseline design.
- Sec. 5, *Reacting CFD of AM-enabled features*, the various AM-enabled features are compared in CFD in terms of some key metrics. The results are summarized and discussed.
- Finally, Sec. 6, *Conclusions*, reviews and summarizes the combustor performance improvements enabled by AM-enabled design features.

2. Methods

This section first describes the methods used to design the baseline combustor against which the later combustor designs are assessed, and then describes the additively manufactured features that appear in those designs.

2.1. Design and analysis of baseline combustion chamber

The following subsections explain the reasoning behind the combustor technology choice and architecture, and the methods used for combustor sizing, airflow distribution, fuel injector design, and swirler sizing.

2.1.1. Initial design decision

The first decision made in this research project concerned the type of low emissions combustor technology to be used as the basis for development of suitable AM features. Several dry low-NOx emissions technologies were considered, all of which aim to control the flame temperature without the use of diluents. This is not an easy task due to the NOx-CO trade-off, shown in Figure 1, such that there is only a narrow temperature window in which both low NOx and CO emissions are attained.
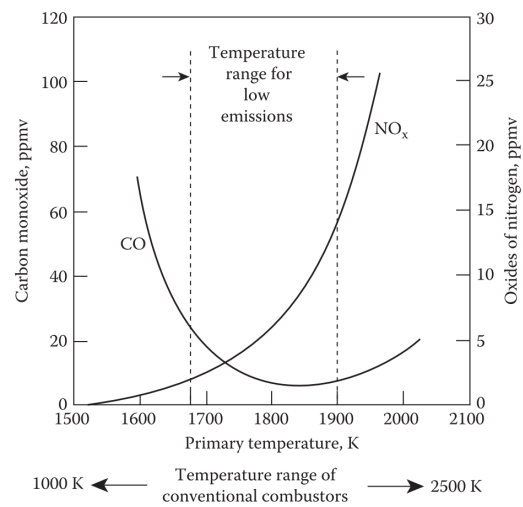

Fig. 1 – Influence of primary-zone temperature on CO and NOₓ emissions [20].

Other factors that affect emissions include the flame structure and the combustion product residency times which can be controlled with the use of geometries that alter the internal aerodynamics of the combustion chamber. After extensive background research, several technologies were identified that could meet the desired specifications presented in Table 1. These include trapped vortex combustion which uses internal cavities to create a vortex of products and reactants with high residency times to allow for more complete combustion, leading to lower emissions [21].

Flameless combustion was also considered since it reduces the flame temperature by increasing the temperature of the reactants past their self-ignition temperature while also entraining enough inert combustion products to create an almost uniform heat release with very low emissions. An example of a Turbec T100 being modified for flameless combustion can be seen in ref. [22], with further reading on micro gas turbines available in references [23] and [24].

The final technology considered was lean premixed combustion. It uses well mixed air-fuel mixtures at the lowest sustainable equivalence ratios and strong recirculation zones to create a low-temperature stable flame.

Applications of this can be found in MTTs Mk5 combustor [25], the Turbec T100 [26], and the US Navy's Black Ghost engine [27].

The decision was made to use lean premixed combustion as the basis for the current prototype for two reasons. Firstly, it is the simpler and more well-established technology. Secondly, and most importantly, it has the highest potential for improvement, by employing AM features to enhance air-fuel mixing and provide a more effective flame stabilizer geometry.

The next step was to select the chamber architecture. A single can-type combustor was chosen due to the desire to create a modular test rig, which would be impractical with any other type of geometry, such as an annular or tuboannular combustor, examples of which can be seen in Figure 2. Nonetheless, much of the learning from the single can combustor can be applied to the other geometries.
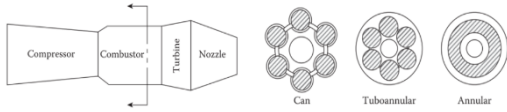

Fig. 2 – Illustration of three main combustor types [20].

In terms of introducing air into the combustor there are generally two approaches, as can be seen in Figure 3. The first is an axial flow arrangement where all the air enters through the front of the chamber and is then distributed through the various passageways, diffusers, and flame stabilizers, such as swirlers and bluff bodies. The second is reverse-flow arrangement where the air is introduced through the casing at the rear of the combustor and flows to the front before making an abrupt turn and flowing axially back out. The latter was chosen based on its expected benefits, which include low frontal area requirement, making the possibility of mounting the compressor and turbine wheels closer together, which is required in small engines due to the high shaft speed, while coupling the reverse flow architecture with a tubular chamber makes inspection and servicing much easier.

The final decision for the baseline combustor concerned the type of flame stabilizer to be employed. There are a wide variety of geometries and mechanisms that can create a stable flame, such as the use of bluff bodies or opposing air and fuel jets to create recirculation zones, the inclusion of wall recesses to entrap fresh and burnt products, and the use of pilot flames to create a stable base for the flame. However, the decision was made to use a swirler to generate a strong recirculation region in the primary zone of the combustion chamber. A swirler will provide enhanced mixing compared to bluff bodies or other means, because the swirl components create strong shear regions, high turbulence and rapid mixing, all of which benefit the stability and intensity of combustion [20]. The two main types of swirlers can be seen in Figure 4. Axial swirlers operate by admitting air axially and passing it though angled vanes to generate swirl, while radial designs have a tangential air feed with either flat or curved vanes for swirl generation.

(a)
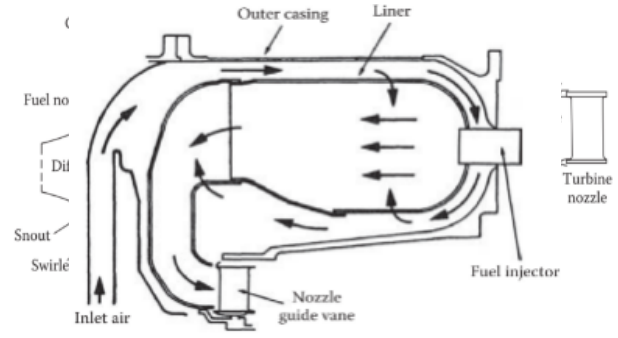
(b)

Fig. 3 – (a) Axial and (b) reverse air flow architecture [20].

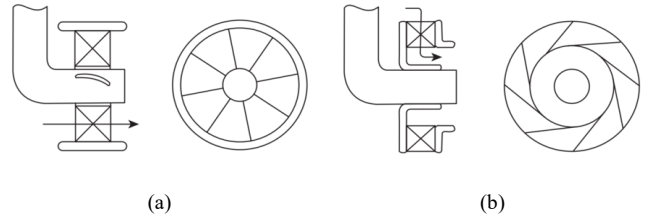(a)   (b)

Fig. 4 – (a) Axial and (b) radial swirler [20].

A radial swirler is the better option for a can-type combustor architecture since it allows for a more compact design while enabling easier modifications through the use of AM. The application of AM techniques to axial vanes would have been more difficult since they depend on free-standing sharply angled features, which are not easy to produce using AM.

Another objective of this research project was to increase the service life of the combustion chamber. To achieve this, the development of an AM cooled liner was undertaken. Augmented backside cooling was considered for this enhancement since it allows further conservation of air which would otherwise be required for cooling purposes. This approach also minimizes emissions formed in the primary zone, which have been seen to increase with the use of film cooling, demonstrated in [28], where Transply (multilaminate high-temperature alloy sheet) was tested on a small radial can combustion chamber.

2.1.2. Combustor sizing

The first step in the baseline design was to size the combustor liner and casing diameters and lengths. Equation 1 [29] was used to find the reference area, A_{ref}, which is also the frontal area of the chambers casing. This also allows for the casing diameter to be calculated.

$$A_{\text{ref}} = \left[R_a \left(\frac{\dot{m}_3 \sqrt{T_3}}{P_3} \right)^2 \left(\frac{\frac{\Delta P_{3-4}}{q_{\text{ref}}}}{\frac{\Delta P_{3-4}}{P_3}} \right) \right] \tag{1}$$

The gas constant R_a was set to 143.5 J · kg^{-1} · K^{-1}. Appropriate values for the normalized total pressure loss $\Delta P_{3-4}/P_3$ and pressure loss factor $\Delta P_{3-4}/q_{ref}$ are based on data provided by Lefebvre [20], listed in Table 2.

The rest of the values such as the mass flow and pressure were set based on the project specifications in Table 1. Although chemical considerations could also be used to calculate A_{ref}, in general, if it is sized for a certain pressure loss, as in this case, it will also accommodate the chemical reactions required; this was again based on the work of Lefebvre [20].

Table 2 – Pressure losses in combustion chambers [20]

Type of chamber	$\dfrac{\Delta P_{3-4}}{P_3}$	$\dfrac{\Delta P_{3-4}}{q_{ref}}$	$\dfrac{m_3 T_3^{0.5}}{A_{ref}P_3}$
Tubular	0.07	37	0.0036
Tuboannular	0.06	28	0.0039
Annular	0.06	20	0.0046

The liner area was simply determined using Sawyer's suggestion [29], that the liner to reference area ratio should be 0.7, which in turn also provides the liner diameter. Slight adaptations to the casing and liner diameters were then made to accommodate the use of commercially available materials.

The initial length of the primary and dilution zone was determined using some basic assumptions based on Sawyer's [29] and Lefevre's design guidelines [20]. Sawyer suggests a primary zone length of either 2/3 or 3/4 of the combustor diameter and Lefebvre suggests a dilution length of 1.5–1.8 times the inner diameter of the combustor. The longer length for the primary zone was chosen, since a longer primary zone should allow for longer residency times, leading to lower emissions. The initial dilution length is determined by considering the required pattern factor Q, which is calculated using Equation 2, where T_{max} is set to the maximum temperature the material can withstand, which for Inconel 625 is 1290 °C.

$$Q = \frac{T_{max} - T_4}{T_4 - T_3} \qquad (2)$$

Using the value of Q calculated, the previously chosen pressure loss factor, and the appropriate equation from Table 3, an initial dilution zone length of 155 mm was determined, which lies within Lefebvre's suggested range.

Table 3 – Dilution zone length to combustor diameter ratio as function of Q for different values of Pressure Loss Factor

$\Delta P_{3-4}/q_{ref}$	L_{DZ}/D_L
15	$3.78 - 6Q$
20	$3.83 - 11.83Q + 13.4Q^2$
30	$2.96 - 9.86Q + 13.3Q^2$
50	$2.718 - 12.64Q + 28.51Q^2$

2.1.3. Airflow distribution

Having determined the approximate size of the combustion chamber, the next step is to arrange for the distribution of air within. A typical combustor has multiple locations where air is distributed, which can be separated into three main zones. The primary combustion zone, where the air and fuel will react and release the required thermal energy; the dilution zone, where fresh air is admitted to reduce the temperature of the hot gases to an acceptable level before it enters the turbine wheel; and a third, smaller zone to collect the air that is used to cool various parts of the combustion chamber (primarily the inner liner, since this experiences the most extreme thermal conditions).

Due to the decision to use augmented backside cooling for the inner liner, the air for this design was assumed to be split evenly between the primary and dilution zones since no excess air is required for liner cooling. With this information and the assumption of a 3% pressure drop between the annulus and the inner combustion chamber, which I based on the design specifications, the dilution holes could be sized. The most common design methods for dilution holes are the Cranfield and NASA methods. The Cranfield method was used here since it focuses primarily on hole size rather than spacing (as in the NASA method). A detailed guide on how to perform this method can be found in Lefebvre's book [21].

2.1.4. Fuel injector design

For the baseline design, it was decided that the fuel injection would occur within the swirler passageways. This decision was based on work conducted on low NOx combustors by Andrews & Kim [30] and on radial swirlers by King et al. [31], which achieved single-digit ppm NOx, CO and THC emissions with swirler embedded injection in a radial swirl-stabilized can combustor. Alterations to the design in these referenced works included the shape of the injector, which in this case was designed using an airfoil style structure. The airfoil shape is designed to generate a small recirculation zone in its wake to help with mixing while keeping pressure loss at a minimum.

Further alterations to the referenced design include the shape of the injection holes, which are two teardrop-shaped orifices facing the sidewalls of the swirler passageway. The teardrop shape ensures each orifice can be printed accurately and without faults since they would be formed in the build direction, meaning the top half of the hole would not be an overhang. The size of the teardrop feature was kept to a minimum based on the industrial partner's experience in generating the smallest accurate orifice possible without the need for post-processing. The smaller the orifice, the greater the fuel jet penetration into the high-velocity air flow in the swirler passages, but not so small as to incur poor surface finish, since no post-processing would be possible on these internal features, which are inaccessible by tools.

The injector design can be seen in Figure 5, where the bottom left figure is a top-down view of a single swirler vane, and the right-side figure is a projection of the curved cutline down the centre of the vane. Annotations to visualize the air and fuel flows are also included. The integrated fuel plenum can also be seen here, which was included to help ensure even fuel distribution to all the injectors while also absorbing heat through conduction from the combustion chamber.
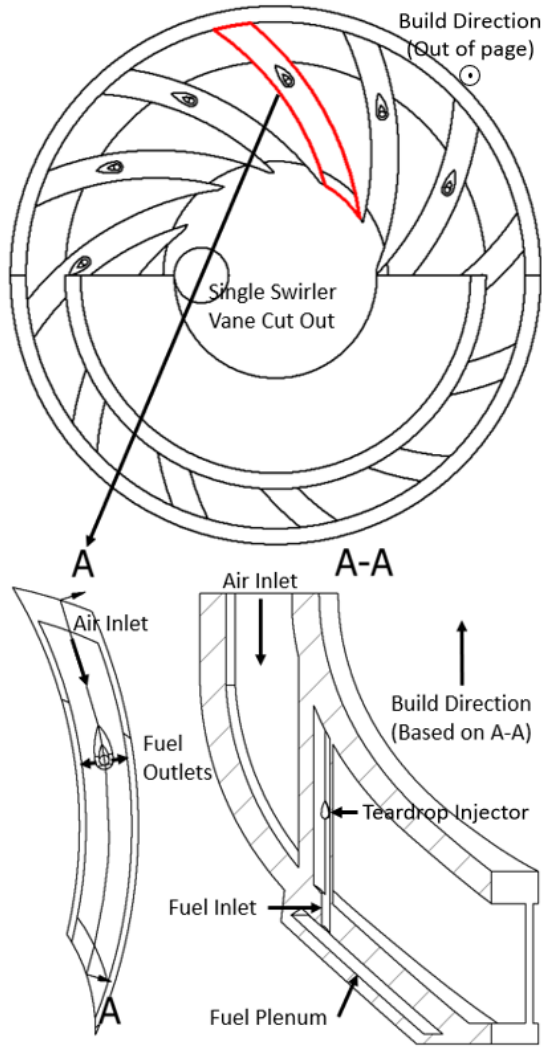
Fig. 5 – In passage fuel injector design.

2.1.5. Swirler sizing

The swirler was designed to meet three criteria. The first was the creation of a strong recirculation in the primary zone, which was key to the creation of a steady flame while also ensuring that emissions are kept low by maximizing mixing and unburned combustion product residency time. To quantify the recirculation strength, the swirl number was calculated which is a non-dimensional number characterizing the amount of rotation imposed on the flow. Based on the work conducted in ref. [32], a swirl number of at least 0.6 is recommended for the creation of a satisfactory primary zone flame. To generate the initial design, the swirl number formula derived and validated in ref. [32], shown here in Equation 3, was used, as it requires only geometrical data.

$$S_{\mathrm{g}} = \frac{r_{\mathrm{o}} \pi r}{A_{\mathrm{t}}} \left(\frac{\tan \vartheta}{\tan \vartheta + 1} \right)^2 \qquad (3)$$

Where A_t is the area of the tangential inlets, r is the radius of the exit of the combustor and r_o is the radius of the tangential inlets of the combustor. The $\tan \vartheta$ and $\tan \vartheta + 1$ represent the tangential and total flow at the plane used for the measurement of the swirl number.

The second design criterion was the prevention of flashback. Due to the desire to partially premix the air and fuel in the swirler, the issue of flashback inside the passageways must be addressed. Generally, flashback occurs when the flame velocity exceeds the approaching mixture velocity. This leads to the flame propagating upstream of the combustion zone and back into the premixing zone, which tends to lead to damage in the combustor, although there are other contributing factors that lead to flashback. The three main types of flashback mentioned in ref. [20] are as follows. Firstly, free-stream flashback. The second type is flashback which generally occurs in the low-flow velocity located in the boundary layers along the walls of the premixing section, and the third which only applies to swirl-stabilized combustors, is combustion-induced vortex breakdown (CIVB). Useful descriptions of the three flashback mechanisms can be found in the works by Plee & Mellor [33] and Kiesewetter et al. [34].

To prevent flashback from occurring, a strong recirculation is required to combat CIVB, which, as previously mentioned, is required for a multitude of other reasons. To address the free steam velocity mechanism of flashback, the laminar flame speeds for a range of equivalence ratios at a constant inlet temperature and pressure, and employing the methane properties from GRI-Mech 3.0, which is an optimized mechanism designed to model natural gas [35], were input into a combustor reactor model in CHEMKIN-PRO [36]. In the baseline design, the flashback mechanism caused by retarded flow along the wall was not addressed, although this was kept in consideration when AM features were added later.

The third and final design criterion for the swirler was the minimization of pressure loss. This is a common drawback for radial swirlers with internal fuel injection since the required features to ensure good mixing and high velocities through the vanes tend to lead to an increase in pressure loss. This was addressed by using AM features which are described in the following section.

2.2. Additively manufactured features

The next subsections explain general guidelines for design for additive manufacturing, followed by design considerations specific to the novel combustor features developed in this work, such as the conical swirler, the lattice structures used for mixing, and the backside cooling mixer.

2.2.1. Additive manufacturing design guidelines

As with all manufacturing methods, the limitations of AM must be considered during the design process to avoid issues during manufacturing. Indeed, this project pushed the limits of the AM machines while trying to reduce the likelihood of build failures.

The first and most well-known limit is the build angle at which any given feature can be built unsupported. This is typically 45° from vertical, although angles up to 50° have been achieved, albeit with varying quality. Although it is possible to print designs having small overhangs at any angle (up to approximately 1 mm in length unsupported, longer if removable supports are used), for this project it was decided not to rely at all on internal supports, in order to minimize post-processing and reduce build

complexity. This meant that the flame stabilizing design concepts and the overall geometry of the combustor were purposely chosen to avoid the compromises that arise in an unsupported design, such as reduced surface quality or a redesign which sacrifices performance. Examples of this design approach can be seen in Figure 5, which shows the swirler's internal passageway injector and fuel plenum, which are self-supporting features.

When designing the fuel injector, another limitation considered was the minimum hole size that can be built consistently and with a good surface finish. Based on AM build parameters available at the time of manufacture for Inconel 625, which was used for all of the combustors AM parts, it was decided a hole of 0.75 mm diameter was the smallest that could be achieved whilst maintaining good dimensional accuracy. Both the fuel inlet and outlet holes that can be seen in Figure 5 were specified in this size. However, due to its orientation, the outlet hole employs a teardrop shape to avoid build defects often found with holes perpendicular to the build direction; in other words, the teardrop design avoids any overhang.

2.2.2. Conical swirler

As previously mentioned, one of the main design criteria for the swirler was the minimization of pressure loss. Typically, the inlets of a radial swirler are orientated at a 90° angle to the incoming airflow, as seen in Figure 4. This causes increased pressure loss due to flow separation in these areas, an example of which can be seen in ref. [31], where CFD and water flow were used to visualize the swirler inlet aerodynamics. To alleviate this issue, the authors angled the swirler vanes and passageways towards the airflow to minimize flow separation at the entrance to the swirler.

To ensure a smooth transition of the airflow from the combustor annulus to the swirler passageways, radii were added to the guide vanes. Figure 6 highlights the conical shape of the swirler (R5 and R6) and the radii on the swirler vanes (R7); the corresponding dimensions are listed in Table 4.
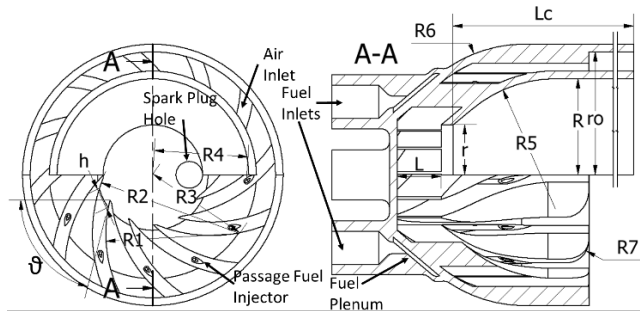

Fig. 6 – AM radial swirler and combustor configuration.

Table 4 – Radial swirler and combustor dimensions

Specifications	Values	Units
Number of vanes	12	
ϑ	45	°
R1	35	mm
R2	38.5	mm
R3	27.4	mm
R4	24.5	mm
R5	34	mm
R6	36	mm
R7	6	mm
R	25	mm
ro	32	mm
R	13	mm
H	3.5	mm
L	11.5	mm
At	483	mm^2
S	0.68	
Lc	225	mm

2.2.3. Lattice structure mixer

As previously mentioned, the baseline combustor aims to use a lean premixed air-/fuel mixture to control the primary zone temperature and consequently the emissions generated. A key prerequisite for successful premixed combustion is a high quality of mixing of air and fuel. This can be achieved in many ways, including but not limited to premixing in a large chamber before injection, using the surrounding aerodynamics to create a mixing region, or with the use of geometric features.

Since the goal of this project is to highlight the possibilities that AM reveals for combustor design, it was decided that the use of a lattice structure to encourage better mixing would be an interesting feature to investigate.
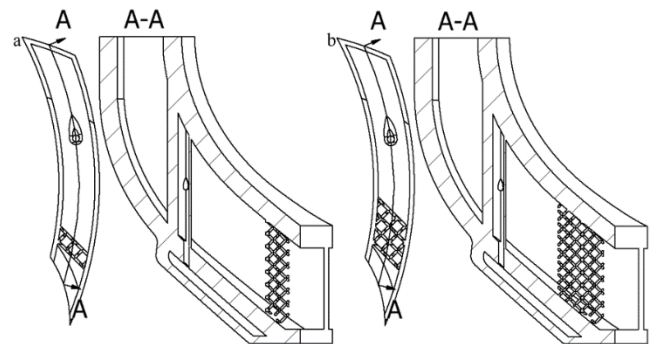

Fig. 7 – (a) One-row internal lattice; (b) Three-row internal lattice.

This lattice structure was implemented downstream of the fuel injector at the exit of each swirler passageway to enhance mixing by generating turbulence around the lattice beams. As can be seen in Figure 7, two geometries were created. The first (Fig. 7(a)) is a single-row lattice structure consisting of a cube vertex centroid with 0.3 mm diameter beams and a 1.8 mm cube. Although this was not the smallest achievable unit cell size, based on prior experience with AM build parameters available at the time of manufacture, it could be generated reliably and with minimal chance of blocked cells (that would drastically increase backpressure). To investigate the effect of increasing the volume of the mixing surfaces, a

three-row lattice structure was also generated (Fig. 7(b)). In either case, the lattice structure was generated by creating a simple unit cell in Autodesk Inventor, which was then patterned and cut to fit the swirler passageway.

2.2.4. Upstream augmented backside cooling mixer

Augmented backside cooling surfaces were developed to showcase the capability of AM to create a combustor liner that offers excellent cooling effectiveness with minimal pressure loss. This also presented the opportunity to investigate a potential secondary use for the surfaces as a region for premixing. This was achieved by creating a fuel ring, shown in Figure 8, with four inlets and multiple teardrop-shaped outlets to evenly distribute the fuel around the annulus of the combustor, upstream of the backside liner cooling fins, as shown in Figure 9. This choice of positioning encourages mixing while avoiding flow of fuel into the dilution holes.
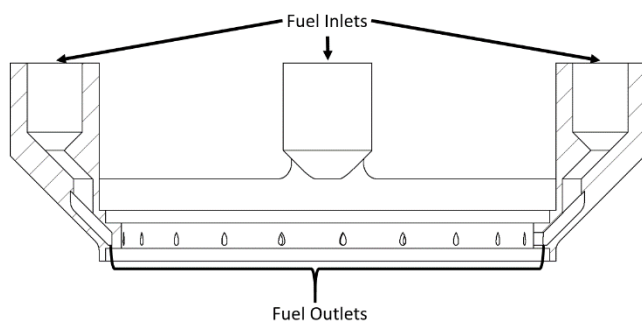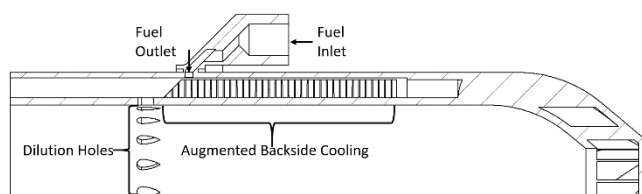

Fig. 8 – Upstream fuel ring

Fig. 9 – Upstream injection geometry.

The surface used for the upstream fuel mixing is a curved fin designed to increase the cooling surface area by rotating a straight fin around the periphery of the liner, which would also be preconditioning the flow using the curved fin to impart some swirl and thus achieve better alignment at the inlet to the swirler itself. Although it is not the primary function of the liner to operate as a fuel and air mixer, because it has incoming airflow it was considered that it could potentially be a secondary use for it. The surface can be seen in Figure 10 with its basic dimensions presented in Table 5. As already mentioned, a previous publication of this author [37] covers its design and the subsequent testing of its cooling effect.

Table 5 – Curved Fin Dimensions

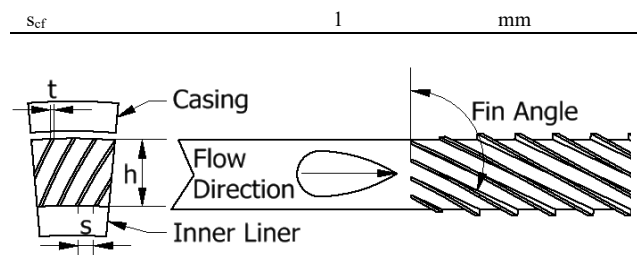| Dimensions	Values	Units
ϑ_{cf}	35	°
t_{cf}	0.2	mm
h_{cf}	4	mm

s_{cf}	1	mm

Fig. 10 – Curved fin geometry

2.2.5. Flat swirler

For the purposes of the CFD comparison reported later, a flat swirler model was created (Figure 11), using vane and fuel injector dimensions identical to the conical swirler in Figure 6. Such a design can be made by traditional manufacturing methods and so provides a reference point against which the AM-enabled designs can be compared. The main differences in the flat swirler are that the vanes do not begin in the annulus and are not curved towards the incoming air flow from the annulus.
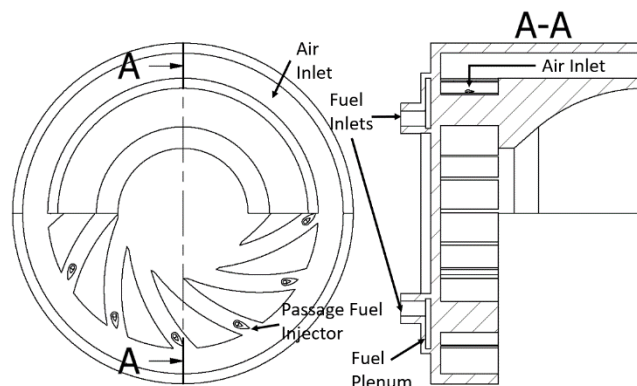
Fig. 11 – Flat swirler configuration.

3. Results and Discussion

This section reports reacting CFD simulations results, first for the baseline combustor design and secondly for the additively manufactured features.

3.1. Baseline reacting computational fluid dynamics, manufacturing and validation

The next subsections report reacting CFD simulation results for the baseline combustor, with validation against experimental test data.

3.1.1. General setup

To simulate the reactions occurring inside the different combustion chamber design a flamelet model was used, as this avoids the computational expense of complex chemistry calculations. Instead, the gas-phase laminar flame chemistry is pre-calculated using simple 0D or 1D geometries, by employing detailed reaction mechanisms. In this case, STAR CCM+

2020.1 was used for the full-scale 3D CFD modelling, and which offers a Flamelet Generated Manifold (FGM) model, which is generally regarded as the most accurate flamelet model for steady-state combustion chambers. The FGM stores the detailed combustion chemistry in a flamelet table from which the required values are retrieved during the CFD simulation. A progress variable facilitates the interaction between the main CFD simulation and the flamelet table.

During the generation of the flamelet table, details on the chemical mechanisms that can occur are required; these are sourced from the GRI-Mech 3.0, which is an optimized mechanism designed to model natural gas combustion, including NO formation and reburn chemistry which is made up of 325 reactions and 53 species [35]. To predict the NOx emissions thermal and Zeldovich models were used. A simulated ignitor was also used, where a small volume of the combustor is set to a temperature capable of igniting the air-fuel mixture for a small number of iterations, this allows for a more accurate representation of where the flame would sit after it is ignited using a spark plug or other source of ignition.

RANS modelling was used as it offers a sensible compromise between accuracy of the steady-state simulations (reported later) and computational expense. For turbulence modelling, Menter's k-ω SST model [38] was used with 2nd order segregated fluid enthalpy.

The boundary conditions were based on the lab testing measured inputs. The air and fuel inlets were set as mass flow boundaries, while the outlet boundary was set as a static pressure. The main boundary condition settings are presented in Table 6.

Table 6 – CFD boundary conditions

Location	Parameter		Value	Units
Air Inlet	Mass flow rate	$\dot{m}_a$	70	g/s
	Temperature	T_a	820	°C
Fuel Inlet	Mass flow rate	$\dot{m}_f$	0.674	g/s
	Temperature	T_f	60	°C
Outlet	Pressure	P_{out}	400	kPa
	Temperature	T_{out}	1250	°C

A polyhedral mesh was created for all combustor geometries, employing variable cell size according to the complexity of the reacting flow. Indeed, the variation in mesh density can be inferred from the changing opacity of the section view of the baseline geometry mesh in Figure 12, which also displays the locations of the air and fuel inlets, and the combustor outlet. The mesh is made up of approximately 10 million cells, with more complex geometries leading to a higher cell count.
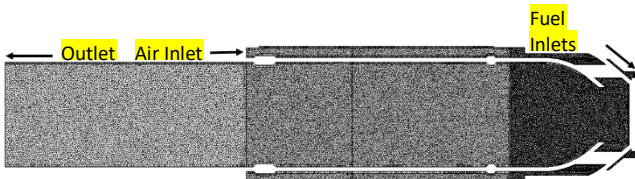

Fig. 12 – Section view of baseline geometry mesh

3.1.2. Conical swirler validation (Baseline)

To build confidence that the baseline design would be suitable for lab testing, CFD predictions were compared to the design specifications.

3.1.2.1. Temperature

Figure 13 shows the CFD-predicted temperature field on the midpoint axial-radial plane, in which a maximum of 1540°C is attained at the operating conditions displayed in Table 6. This lies in the middle of the low-emission temperature window identified within the NOx-CO trade-off in Figure 1, hence one may reasonably expect low emissions of both NOx and CO from the baseline combustor.
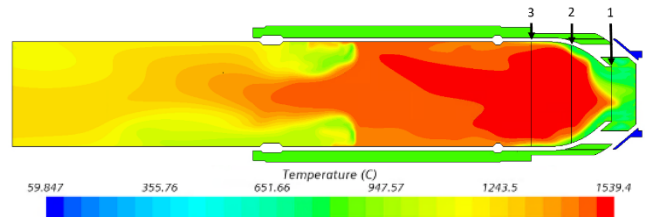

Fig. 13 – Predicted temperature field for the baseline combustor

The regions of peak temperature also provide an estimation of flame location, viz. just above the swirler throat exit. One may also observe the highest temperature regions do not touch the combustor walls, which will help extend combustor life by reducing metal temperatures.

The locations of three section planes are also identified in Figure 13. These will be used later in the estimation of the swirl number, while Location 1 will also be used to compare equivalence ratios between different geometries to evaluate the fuel mixing enhancements.

At the combustor outlet, a mass flow-average temperature of 1184°C is predicted, which is lower than the desired 1250°C in the specification. This is most likely due to an excess of dilution air, which can be adjusted by reducing the dilution flow area.

3.1.2.2. Pressure loss

The pressure loss across the combustor is calculated as the difference between the predicted inlet and outlet static pressures. For the baseline, this was found to be approximately 13.5 kPa, which is very close to the target specification of 3% of the inlet pressure (400 kPa).

3.1.2.3. Swirl number

As mentioned, a swirl number of approximately 0.6 promotes a stable flame structure while reducing emissions by increasing the residence time of the unburnt products. The swirl number at each of the three aforementioned locations (Fig. 13) was calculated using the method provided in the STAR-CCM+ resource library, and which is outlined next.

The base equation used for the swirl number (S) in CFD is presented in Equation 4, where vt, va, V, A, and R are the tangential and axial components of the velocity vector, the velocity vector itself, the flow area, and the hydraulic radius, respectively.

$$S = \frac{\int r v_t \vec{V} . \overrightarrow{dA}}{R \int v_a \vec{V} . \overrightarrow{dA}} \qquad 4$$

For use in STAR-CCM+, Equation 4 is discretized as Equation 5, where A_n is the area of the cell normal to cylindrical coordinate axis. The summation operator in Equation 5 applies over all cells in the plane for which the swirl number is being calculated.

$$S = \frac{\sum\{v_t \, r \, V \, A_n\}}{R \sum\{v_a \, V \, A_n\}} \qquad 5$$

The next step is to define a cylindrical coordinate, since Equation 5 operates on the axial and tangential components of the velocity vectors. Multiple field functions are then defined for each part of Equation 5. Three summation reports are also created for the section radius, and both the angular and axial momentum flux. The final step is the creation of a surface average report using the swirl ratio number function to generate a single swirl number for the plane in question.

The results for the baseline design can be seen in Table 7. At the base of the flame (Location 1) the swirl number is higher than targeted but reduces to just below 0.6 further into the combustor (Locations 2 and 3).

Table 7 – Swirl Number

Configuration	Location 1	Location 2	Location 3
Conical swirler	0.88	0.51	0.57

3.1.2.4. Equivalence ratio

A strong indicator of how well the air and fuel are mixed is the equivalence ratio (the ratio of the actual to stoichiometric fuel-air ratios). The CFD-predicted equivalence ratio is reported at the exit of the swirler throat (Location 1 in Figure 13), such that the mixture quality could be quantified by recording the maximum value on the corresponding plane.

In Figure 14 a cut-plane at Location 1 can be seen, where the fuel is concentrated in a ring near the outer edge of the combustor. This ring slowly dissipates as the mixture makes its way through the combustor's primary zone and follows a similar axial path to the flame front seen in Figure 13.
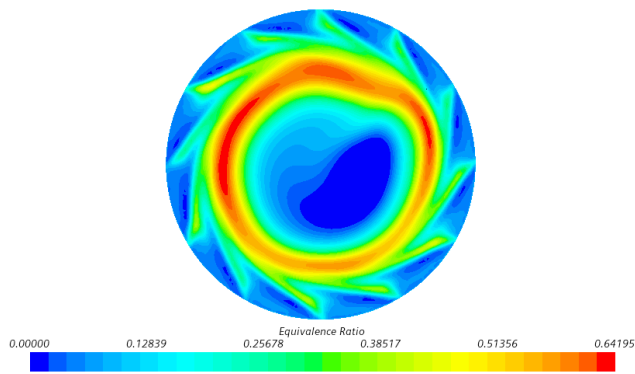

Fig. 14 – Swirler throat exit (Location 1) equivalence ratio

3.1.2.5. Emissions

The final parameters used to compare the baseline design to the rest of the geometries are the NOx and CO emissions. These are of great importance since the main goal of this project is to design and demonstrate

AM-enhanced combustor features that generate ultra-low emissions, in the current global push for clean power generation.

Figure 15 displays the mass fraction of CO. While there are low levels of CO predicted at the flame front, these become insignificant at the outlet.
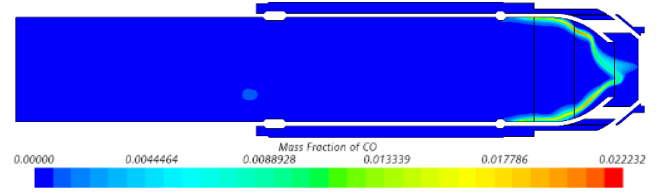

Fig. 15 – Primary zone CO emissions

Figure 16 shows the NOx emissions distribution through the centre of the combustion chamber. As expected, the NOx is at its peak in the primary zone, where the flame temperature is highest and then dramatically decreases once the dilution air is introduced which drops the overall temperature. At the outlet of the combustor, a mass flow average value of approximately 6 ppm was predicted, indicating the design would provide low enough emissions to meet the design goals.
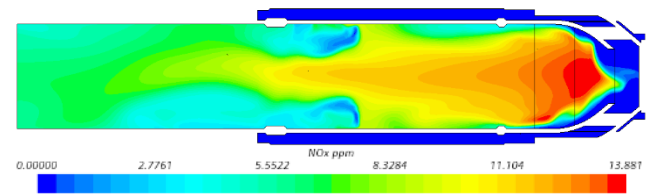
Fig. 16 – Primary zone NOx emissions

3.1.3. Manufacturing, parameters, and materials

The next step of the project was the manufacturing of the CFD-assessed baseline design. Renishaw AM250 and AM500Q machines were used to build the various combustor parts, depending on their availability. The main difference between them is that the AM250 uses a single 200 W capable ytterbium fibre laser [39], while the AM500Q uses four lasers each capable of 500 W [40]. The AM500Q also has improved optics and gas flow distribution as it is a newer model.

Figure 17 shows the AM500Q build chamber, with the argon purge gas inlets located on the bottom right, the laser outlet on the top, and the re-coater and powder dispenser at the back of the chamber. The chamber's build plate has a build area of 250 mm square, with four mounting holes and a typical thickness of 25 mm, although 50 mm thick plates are available for larger parts. The maximum build height of the chamber is 350 mm for the AM500Q (300 mm for the AM250).

Fig. 17 - AM500Q build chamber [41].

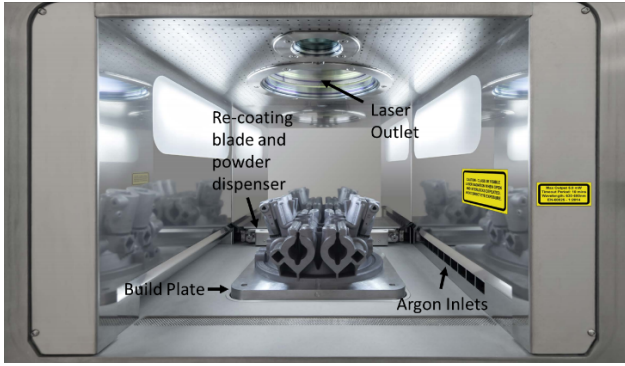For all the combustor parts, Inconel 625 nickel superalloy was used. This material selection was based on the available materials that the industrial partner could supply and how well they would handle the demanded pressures and temperatures. Other materials considered included Inconel 718, but due to its yield strength dropping off at a lower temperature when compared to Inconel 625 it was not selected [42]. Hastelloy X was also considered due to its exceptional creep resistance at high temperatures but was not available at the time of manufacture[43]. The powder used is similar to the Renishaw specification [44]. Typically, the powder has a 15–45µm particle size range, with inspection carried out at the supplier. This is checked again if any issues arise during a build.

The same build parameters, shown in Table 8, were used for either printer, they were the latest released build parameters available at the time of manufacture. For the hatch scanning strategy, alternating paths at a 67° angle are used to reduce laser sintering repetition on each layer.

Table 8 – Build parameters

Parameter	Laser Power	Scanning Speed	Layer Thickness
Values	200 W	900 mm/s	60 µm

3.1.4. Post-processing

The first post-processing step is typically the removal of the non-sintered powder. This was completed using a shaker table that has high- and low-frequency settings. Once this process is completed, which can take up to several days depending on the complexity of any internal passageways, the next step is to heat treat the parts. For Inconel 625, the heat treatment process lasts one hour at 1050°C.

For ease of removal from the build plate, all parts were printed on supports. These were shaped to fit the building base of the part and had a saw blade-like interface profile to minimize the removal force required. An example can be seen in Figure 18, where four swirlers are presented on the plate as they came out of the printer. To further minimize the post-processing time all threaded holes were printed, only requiring a finish tapping. This faster procedure only slightly compromises thread quality.

Fig. 18 – As-printed swirlers.

3.1.5. Computational fluid dynamics validation

To ensure the CFD comparisons of the AM features were an accurate representation of the future test results, early laboratory testing was completed on the baseline AM combustor to gather results to validate the reacting CFD model. For brevity of this paper, only a short description of the laboratory test setup and the accuracies of the equipment used will be presented here, with a more detailed description being included in a future publication with the rest of the laboratory results.

Figure 19 shows the test cell setup for this research. Two electric heaters were used in conjunction with multiple heat exchangers to provide the required combustor inlet air flows and temperatures to reach the desired operating conditions. The pressure of the system was controlled using an electronic butterfly valve, with additional pressure control achieved via the secondary air injected downstream of the exhaust, which also reduced the exhaust gas temperature to acceptable levels.
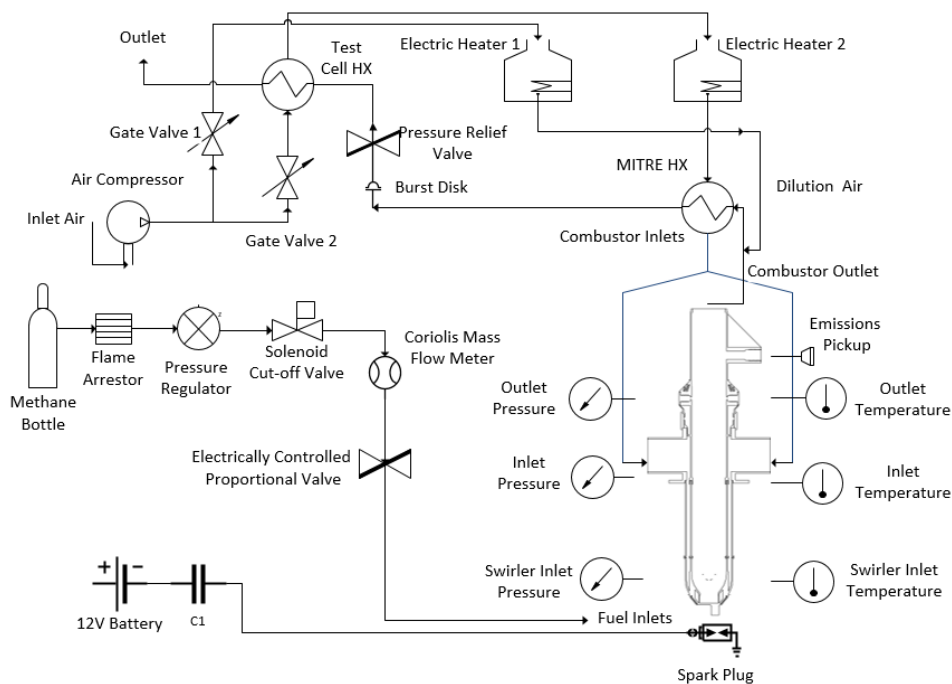
Fig. 19 – Laboratory test cell schematic

The fuelling of the combustor was controlled using an electronic proportional valve, with the mass flow rate of fuel measured by a Coriolis meter, both of which were attached to a pressurised methane gas bottle with a pressure regulator to reduce bottle pressure from 200 to 5 bar. Ignition of the combustor was achieved with the use of an operator-controlled 8 mm spark plug connected to a capacitor powered by a 12V battery. A list of all experimentally measured parameters, the corresponding sensors and uncertainty ranges can be found in Table 9.

Table 9 – Experimentally measured parameters

Parameters	Sensor type	Sensor accuracy
Combustor inlet and outlet temperatures; swirler inlet temperature (each)	4 x K type thermocouple	± 2.5°C or ± 0.0075 T
Combustor inlet and outlet pressure; swirler inlet pressure	Omega Pressure transducer	± 100 Pa
Air mass flow rate	Calibrated V-Cone	± 0.5%
V-Cone pressure drop	Pressure transducer	± 16 Pa
V-Cone upstream pressure	Pressure transducer	± 280 Pa
V-Cone upstream temperature	Class A PRT	± (0.15 + 0.002 T)
Fuel mass flow rate	Coriolis flow meter	± 0.25%
Emissions	MEXA analyser	± 1.0% FS or ± 2.0% RS

In Table 10, the results from CFD and a single test point with similar operating conditions is compared. As can be seen, the temperatures and pressure loss are within 5% of each other, indicating good agreement

between the two and providing confidence in the rest of the CFD comparisons. It was also noticed that the emissions are not in agreement since the CFD heavily underpredicted the NOx emissions. This is a known issue when conducting steady state reacting CFD.

Table 10 – Comparison of CFD and laboratory test results

Values	CFD	Test	Units	Difference (%)
Air mass flow	70	72	g/s	0.0
Fuel mass flow	0.674	0.74	g/s	0.6
PZ Equivalence ratio	0.33	0.33		0.0
Air inlet temperature	720	750	ºC	4.0
Maximum flame temperature	1447	1480	ºC	2.2
Average outlet temperature	1103	1050	ºC	5.0
Pressure loss	12.3	12	kPa	2.5
NOx emissions	2	6	ppm	66.7

3.2. Reacting computational fluid dynamics of additively manufactured-enabled features

While the conical swirler has so far shown to be more than capable of meeting the design specification (with some slight alterations), it does not mean that design changes employing AM features would not be beneficial.

Five designs will be compared in this section. These include the baseline conical swirler and the previously introduced flat swirler, which uses identical vane dimensions as the baseline but without its conical shape of the baseline. Indeed, the latter was used to determine the effect of the

conical shape of the baseline design. Conical swirlers with single- and three-row lattice (Figure 7), were the next two designs. These were used to determine the benefit of lattice structures on in-vane mixing. Finally, an upstream fuel injection design was created. This attempted to improve mixing by using the fuel ring shown in Figure 8 at the location displayed in Figure 9, as well as the cooling surface displayed in Figure 10. The swirler for the fuel ring designs used the same geometry as the baseline but did not include the in-vane fuel injection. Table 11 lists the name of each design, the additional features they implement, and in which figure they can be seen.

Table 11 – AM Features of competing designs

Configuration	Features	Figures
(a) Flat swirler	Non conical swirler	11
(b) Conical swirler	Baseline	5, 6
(c) 1-row lattice	In-vane lattice mixing	7 (a)
(d) 3-row lattice	In-vane lattice mixing	7 (b)
(e) Curved fin cooling FI	Upstream fuelling/cooling surfaces	8, 9, 10

3.2.1. Temperature distribution

To compare designs, the same CFD setup as previously described in section 4.1 was used, with the only alteration being the removal of the dilution holes so as not to influence the mass flow entering the primary zone with the change in back pressure resulting from each design change. To counter the lack of dilution, the air mass flow rate was adjusted to half the original value shown in Table 6, since the flow was originally intended to be evenly distributed between the dilution holes and the primary zone.

The first comparison involves the maximum temperatures and the flame temperature distribution in the primary zone. These parameters were due to their sensitivity to the swirl number, mixture quality and fluid flow. Table 12 shows that the lowest maximum temperature was achieved with the use of the one-row lattice design. In fact, this was the only design that had a lower peak temperature than the baseline. As expected, the highest temperature recorded was from the flat swirler design (approximately 100°C higher than the baseline), confirming the importance of the conical swirler shape in reducing flow separation inside the vanes, leading to increased mixture quality. The rest of the designs produced similar temperatures to the baseline, indicating performance improvement from the AM designs.

Table 12 – Maximum temperatures

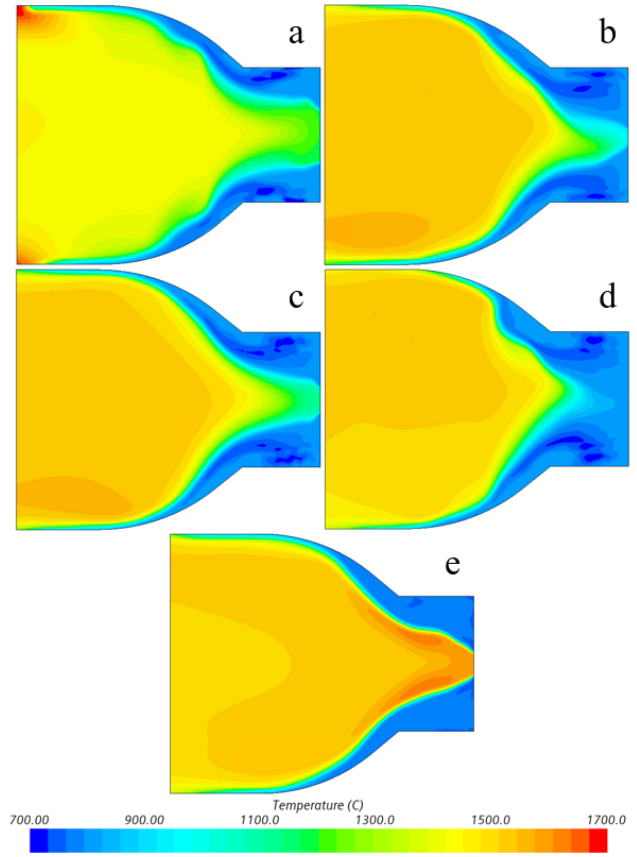| Configuration	Temperatures (°C)
(a) Flat swirler	1722
(b) Conical swirler	1612
(c) 1-row lattice	1548
(d) 3-row lattice	1634
(e) Curved fin cooling FI	1614

Fig. 20 – Primary zone temperature distribution; (a) Flat swirler; (b) Conical swirler; (c) 1 Row lattice; (d) 3 Row lattice; (e) Curved fin cooling FI.

Figure 20 shows the flame temperature distribution for each design, with the correlation to each design being presented via Table 12 and the rest of the CFD results in this section.

The flat swirler displayed a tendency to create local hot spots upstream of the primary zone, as identified in Figure 20(a). This is thought to be due to poor fuel and air mixing, but in general the flat swirler generates a similar flame structure to the rest of the in-vane fuel injection designs. An exception was the three-row lattice Figure 20(d), which had a flame front nearer to the exit of the swirler throat, believed to be due to an increase in turbulence at the exit of the vanes.

A noticeable difference in flame structure can be seen for the upstream fuel injection design Figure 20(e), which shows an increase in the flame front temperature. This could be due to an increase in the pre-mixing of the air and fuel, leading to a more combustible mixture at the flame front, or due to the increase in the fuel temperature, leading to faster reactions at the flame front, or a combination of both.

3.2.2. Pressure loss

Table 13 reports the predicted pressure loss for each design. As expected, the in-vane designs showed the greatest pressure loss due to their location in the highest velocity regions of the combustor. The upstream

fuelling design also showed a higher-pressure loss than the baseline conical design due to the presence of the cooling surface in the combustor annulus.

Table 13 – Pressure loss

Configuration	Pressure loss (kPa)
(a) Flat swirler	1722
(b) Conical swirler	1612
(c) 1-row lattice	1548
(d) 3-row lattice	1634
(e) Curved fin cooling FI	1614

It was also noticed that the conical swirler showed an improvement over the flat swirler, displaying further benefits of the AM design. This is thought to be due to the reduction in flow separation at the entrance of the swirler. This is normally a 90° bend, which would have a greater propensity to cause flow separation at that point.

3.2.3. Primary zone mass flow

As mentioned, for the sake of a fair comparison the mass flow for each design was kept the same by removing the dilution zone as this influences the mass flow split between the primary and dilution zones.

Table 14 shows that the primary zone mass flow is directly related to the pressure loss in each design, with the higher loss designs having lower primary zone mass flow. The only exception was the standard swirler having a higher dilution mass flow than the conical one, but also higher-pressure losses.

Table 14 – Primary zone mass flow

Configuration	Dilution (g/s)	No dilution (g/s)
(a) Flat swirler	36.71	36
(b) Conical swirler	36.52	36
(c) 1-row lattice	33.46	36
(d) 3-row lattice	29.23	36
(e) Curved fin cooling FI	35.22	36

3.2.4. Swirler exit equivalence ratio

Table 15 reports the predicted equivalence ratio at Location 1 for each design. It can be observed that all AM designs significantly improved mixture quality compared to the flat swirler, indicating that the AM features were all working as intended. The upstream fuelling design and the three-row lattice showed further improvement when compared to the conical swirler, suggesting additional benefits from these features.

Table 15 – Equivalence ratio

Configuration	Equivalence Ratio
(a) Flat swirler	1.40
(b) Conical swirler	0.75
(c) 1-row lattice	0.80
(d) 3-row lattice	0.62
(e) Curved fin cooling FI	0.62

3.2.5. Swirl number

Table 16 shows that all AM designs performed similarly in terms of swirl number, except for the three-row lattice, which had a higher initial value. The flat swirler also displayed a lower drop-off in the downstream swirl number, indicating that the mixing features had a minimal effect on the swirl intensity in comparison to the shape of the swirler.

Table 16 – Swirl number

Configuration	Location 1	Location 2	Location 3
(a) Flat swirler	0.78	0.53	0.61
(b) Conical swirler	0.88	0.45	0.56
(c) 1-row lattice	0.85	0.40	0.47
(d) 3-row lattice	0.98	0.43	0.46
(e) Curved fin cooling FI	0.85	0.44	0.53

3.2.6. Primary zone emissions

The predicted emissions levels shown in Table 17 further confirm the superiority of the AM designs. NOx emissions are reduced by 49–75%, and CO concentrations by 22–40%, compared to the traditional flat swirler design.

Table 17 – Primary zone emissions

Configuration	NOx (ppm)	CO (%)
(a) Flat swirler	57	0.032
(b) Conical swirler	14	0.024
(c) 1-row lattice	15	0.019
(d) 3-row lattice	18	0.025
(e) Curved fin cooling FI	29	0.021

Nomenclature

A	Area
AM	Additive Manufacturing
CFD	Computational Fluid Dynamics
CIVB	Combustion-Induced Vortex Breakdown
CO	Carbon monoxide
D	Diameter
FGM	Flamelet Generated Manifold
L	Length
MGT	Micro Gas Turbine
ṁ	Mass flow rate
NOx	Oxides of nitrogen
P	Pressure
r	Radius
V	Velocity
DP	Pressure loss

Subscripts

3	Combustor inlet station
4	Combustor outlet station

Energy Conversion and Management 00 (2021) 000–000

4. Conclusions

This paper reported an investigation into the benefits of additive manufacturing for micro gas turbine combustors. A baseline combustor was designed to meet a target specification using well-known empirical relationships and criteria from the literature. A reacting CFD model of the baseline design, which incorporates a flamelet approach for the combustion chemistry, provided confidence that it would reliably meet the target specification with only minor adjustments to the dilution air split. The CFD model was validated for the baseline combustor, with predictions within 5% of the test data for most parameters. This justified the use of the particular CFD approach for comparing AM features.

Several AM features were implemented to the baseline design to investigate their effect. These included lattice structures placed inside the swirler vanes, and the use of upstream fuelling in the liner cooling surface. A flat swirler was also included to represent a traditionally manufactured (i.e., non-AM) swirler. The same CFD approach, modified only to ensure mass flow rate consistency, was used to compare these five designs.

The CFD predictions found that all AM designs outperformed the flat swirler, both in terms of emissions and the reduction of peak combustion temperatures. This confirms the added value of the AM features in improving combustor performance. In terms of mixing, the upstream fuelling design and the three-row lattice showed significant improvement over the baseline AM design, with a near 20% increase in mixing quality.

In general, all the AM-enabled combustor designs investigated gave similar results in terms of emissions, swirl number, and flame temperature, but at the cost of additional pressure drop compared to the baseline. This was especially the case for the two designs featuring lattice structures. However, any production design would have to include liner cooling surfaces as a means of extending life, so adding the air and fuel mixing functionality might justify the increased pressure loss.

Overall, this work has demonstrated the clear benefits of additive manufacturing for low-emission combustor design. Furthermore, it has introduced a number of novel and very promising AM-enabled design features, exploring the trade-off with pressure drop and quantifying their potential to significantly reduce NOx and CO emissions. Further investigation is warranted into different types of lattice structure and their design optimization to identify the best combination of mixing quality and minimal pressure loss achievable. This could be included as part of a wider topology optimization study at the system level, seeking overall mass reduction, reduction in pressure losses, and increased liner cooling effectiveness.

Acknowledgments

REFERENCES

[1] E. Agelidou, M. Henke, T. Monz, M. Aigner, Numerical Investigation of an Inverted Brayton Cycle Micro Gas Turbine Based on Experimental Data, ASME Turbo Expo 2018: Turbomachinery Technical Conference and Exposition. (2018) DOI: 10.1115/GT2018-76377.

[2] ARPA-E, GENSETS. https://arpa-e.energy.gov/?q=arpa-e-programs/gensets, 2015 (accessed 20 September 2021).

[3] M. Cristina Cameretti, R. Tuccillo, Combustion features of a bio-fuelled micro-gas turbine, Applied Thermal Engineering, 89 (2015) 280-290 DOI: https://doi.org/10.1016/j.applthermaleng.2015.05.057.

[4] H.L. Cao, J.L. Xu, Thermal performance of a micro-combustor for micro-gas turbine system, Energy Conversion and Management, 48(5) (2007) 1569-1578 DOI: 10.1016/j.enconman.2006.11.022.

[5] S. Tuttle, K. Hinnant, M. Vick, Preliminary Design, Ignition, and Fuel Injection for a High Temperature Recuperated Microturbine Combustor, Proceedings of the Asme Turbo Expo: Turbine Technical Conference and Exposition. (2017) DOI: 10.1115/GT2017-63165.

[6] UAVTurbinesInc., UAV Turbines. https://www.uavturbines.com/, 2020 (accesed 20 September 2021).

[7] WRIGHTSPEED, The Route Powertrain. https://www.wrightspeed.com/the-route-powertrain, 2020 (accesed 20 September 2021).

[8] A. Adamou, I. Kennedy, B. Farmer, A. Hussein, C. Copeland, Experimental and Computational Analysis of an Additive Manufactured Vaporization Injector for a Micro-Gas Turbine, Asme Turbo Expo: Turbine Technical Conference and Exposition. (2019) DOI: 10.1115/gt2019-90245.

[9] W.P.J. Visser, S. Shakariyants, M.T.L. de Later, A. Haj Ayed, K. Kusterer, Performance Optimization of a 3kW Microturbine for Chp Applications, Asme Turbo Expo: Turbine Technical Conference and Exposition. (2012) DOI: 10.1115/GT2012-68686.

[10] Bladon Micro Turbine, Bladon MTG Specification. https://www.bladonmt.com/bladon-micro-turbine-genset/bladon-mtg-specification, 2021 (accesed 20 September 2021).

[11] Capstone, C65 :: Capstone Green Energy Corporation. https://www.capstonegreenenergy.com/products/energy-conversion-products/capstone-microturbines/c65, 2021 (accesed 20 September 2021).

[12] General Electric, Transformation In 3D: How A Walnut-Sized Part Changed The Way GE Aviation Builds Jet Engines. https://www.ge.com/news/reports/transformation-3d-walnut-sized-part-changed-way-ge-aviation-builds-jet-engines, 2018 (accessed 20 September 2021).

[13] EOS, 3D-Printed Micro-Burners for Optimized Combustion. https://www.eos.info/en/3d-printing-examples-applications/all-3d-printing-applications/euro-k-industry-3d-printed-micro-burners, 2021 (accessed 20 September 2021).

[14] Siemens, Siemens achieves breakthrough with 3D-printed combustion component for SGT-A05. https://press.siemens.com/global/en/feature/siemens-achieves-breakthrough-3d-printed-combustion-component-sgt-a05, 2018 (accessed 20 September 2021).

[15] O. Andersson, A. Graichen, H. Brodin, V. Navrotsky, Developing Additive Manufacturing Technology for Burner Repair, Proceedings of the Asme Turbo Expo: Turbine Technical Conference and Exposition, Vol 6, 139(3) (2016) DOI: 10.1115/1.4034235.

[16] G. Fantozzi, M. Kinell, S. Rabal Carrera, J. Nilsson, Y. Kuesters, Experimental Study on Pressure Losses in Porous Materials, Journal of Engineering for Gas Turbines and Power, 141(2) (2018) DOI: 10.1115/GT2018-75019.

[17] M. Samoilenko, P. Seers, P. Terriault, V. Brailovski, Design, manufacture and testing of porous materials with ordered and random porosity: Application to porous medium burners, Applied Thermal Engineering, 158 (2019) DOI: https://doi.org/10.1016/j.applthermaleng.2019.113724.

[18] P. Gradl, C. Protz, K. Cooper, D. Ellis, L. Evans, C. Garcia, GRCop-42 Development and Hot-fire Testing Using Additive Manufacturing Powder Bed Fusion for Channel-cooled Combustion Chambers, ASEE Joint Propulsion Conference. (2019) DOI: 10.2514/6.2019-4228.

[19] J. Hahn, Hyperganic uses AI to design 3D-printed rocket engine. https://www.dezeen.com/2020/03/30/hyperganic-ai-rocket-engine-3d-printed/, 2020 (accessed 20 September 2021).

[20] A.H. Lefebvre, D.R. Ballal, GAS Turbine Combustion Alternative Fuels and Emissions, 2010.

[21] D.L. Straub, K.H. Casleton, R.E. Lewis, T.G. Sidwell, D.J. Maloney, G.A. Richards, Assessment of Rich-Burn, Quick-Mix, Lean-Burn Trapped Vortex Combustor for Stationary Gas Turbines, Journal of Engineering for Gas Turbines and Power, 127(1) (2005) 36-41 DOI: 10.1115/1.1789152.

[22] T. Zornek, T. Monz, M. Aigner, Performance analysis of the micro gas turbine Turbec T100 with a new FLOX-combustion system for low calorific fuels, Applied Energy, 159 (2015) 276-284 DOI: 10.1016/j.apenergy.2015.08.075.

[23] M. Khosravy, Review of the New Combustion Technologies in Modern Gas Turbines, in: E. Benini (Ed.), Progress in Gas Turbine Performance, InTech, Rijeka, (2013) DOI: 10.5772/54403.

[24] M.A.R. do Nascimento, L. de, E.C. dos Santos, E.E. Batista Gomes, F.L. Goulart, E.I. Gutirrez Velsques, R. Alexis Miranda, Micro Gas Turbine Engine: A Review, Progress in Gas Turbine Performance, (2013) DOI: 10.5772/54444.

[25] W.P.J. Visser, S.A. Shakariyants, M. Oostveen, Development of a 3 kW Microturbine for CHP Applications, J Eng Gas Turb Power, 133(4) (2011) DOI:10.1115/1.4002156.

[26] M.P. Cadorin, M.; Vaccari, A.; Calabria, R.; Chiariello, F.; Massoli, P.; Bianchi, E., Analysis of a Micro Gas Turbine Fed by Natural Gas and Synthesis Gas: MGT Test Bench and Combustor CFD Analysis, J Eng Gas Turb Power, 134(7) (2012) DOI:10.1115/1.4005977.

[27] M. Vick, T. Young, M. Kelly, S. Tuttle, K. Hinnant, A Simple Recuperated Ceramic Microturbine: Design Concept, Cycle Analysis, and Recuperator Component Prototype Tests, ASME Turbo Expo: Turbine Technical Conference and Exposition. (2016) DOI: 10.1115/GT2016-57780.

[28] G.E. Andrews, M.N. Kim, The Influence of Film Cooling on Emissions for a Low NOx Radial Swirler Gas Turbine Combustor, Asme Turbo Expo: Turbine Technical Conference and Exposition. (2001) DOI: 10.1115/2001-GT-0071.

[29] J.W. Sawyer, Sawyers Gas Turbine Engineering Handbook, Turbomachinery International, 1985.

[30] G.E. Andrews, M. Kim, Small Radial Swirler Low NOx Combustors for Micro Gas Turbine Applications, ASME Turbo Expo: Turbine Technical Conference and Exposition. (2017) DOI: 10.1115/GT2017-63572.

[31] P.T. King, H.S. Al Kabie, G.E. Andrews, M.M. Pourkashanian, A.C. McIntosh, CFD Predictions of Low NOx Radial Swirlers With Central Fuel Injection, ASME Turbo Expo: Turbine Technical Conference and Exposition. (2009) DOI: 10.1115/GT2009-60106.

[32] H.S.A. Kabie, Radial swirlers for low emissions gas turbine combustion, (1989).

[33] S.L. Plee, A.M. Mellor, Review of Flashback Reported in Prevaporizing/Premixing Combustors, COMBUSTION AND FLAME 32 (1978).

[34] F. Kiesewetter, M. Konle, T. Sattelmayer, Analysis of Combustion Induced Vortex Breakdown Driven Flame Flashback in a Premix Burner With Cylindrical Mixing Zone, Journal of Engineering for Gas Turbines and Power, 129(4) (2007) 929-936 DOI: 10.1115/1.2747259.

[35] G.P. Smith, D.M. Golden, M. Frenklach, N.W. Moriarty, B. Eiteneer, M. Goldenberg, C.T. Bowman, R.K. Hanson, S. Song, J. William C. Gardiner, V.V. Lissianski, Z. Qin, GRI-Mech 3.0. http://combustion.berkeley.edu/gri-mech/, 2019 (accesed 20 September 2021).

[36] CHEMKIN-PRO 15112, Reaction Design: San Diego, 2011.

[37] A. Adamou, C. Copeland, Experimental and Computational Analysis of Additive Manufactured Augmented Backside Liner Cooling Surfaces for Use in Micro Gas Turbines, ASME Turbo Expo: Turbine Technical Conference and Exposition. (2020) DOI: 10.1115/gt2020-14960.

[38] F.R. Menter, Two-equation eddy-viscosity turbulence models for engineering applications, AIAA Journal, 32(8) (1994) 1598-1605 DOI: 10.2514/3.12149.

[39] Renishaw, Renishaw AM250 laser melting machine. https://resources.renishaw.com/gen/details/renishaw-am250-laser-melting-machine--38778, 2021 (accesed 20 September 2021).

[40] Renishaw, RenAM 500Q. https://www.renishaw.com/en/renam-500q--42781, 2021 (accesed 20 September 2021).

[41] Renishaw, RenAM 500 series additive manufacturing systems. https://www.machexhibition.com/__media/libraries/pdf-library/E0D29FBE-5056-B725-6B686C96F6E47AD5-document.pdf, 2019 (accesed 20 September 2021).

[42] INCO, Properties of Some Metals and Alloys, The International Nickel Company, Inc., 1982, p. 85

[43] Haynes, HASTELLOY®X ALLOY, Haynes International, Inc., 1997, p. 15

[44] Renishaw, Additive manufafcturing material data sheets. https://www.renishaw.com/en/data-sheets-additive-manufacturing--17862, 2020 (accesed 20 September 2021).